Nano Research
2019, 12(4): 837–844

ISSN 1998-0124 CN 11-5974/O4
https://doi.org/10.1007/s12274-019-2301-3

Research Article

Critical size limit of biodegradable nanoparticles for enhanced lymph node trafficking and paracortex penetration

Gregory P. Howard[1,2], Garima Verma[3,4], Xiyu Ke[2,5], Winter M. Thayer[6], Timothy Hamerly[4], Victoria K. Baxter[3,7], John E. Lee[8], Rhoel R. Dinglasan[3,4] (✉), and Hai-Quan Mao[1,2,5,9] (✉)

[1] *Department of Biomedical Engineering, Johns Hopkins School of Medicine, Baltimore, MD 21218, USA*
[2] *Institute for NanoBioTechnology, Johns Hopkins University, Baltimore, MD 21218, USA*
[3] *W. Harry Feinstone Department of Molecular Microbiology & Immunology, and the Malaria Research Institute, Johns Hopkins Bloomberg School of Public Health, Baltimore, MD 21205, USA*
[4] *Emerging Pathogens Institute, Department of Infectious Diseases & Immunology, College of Veterinary Medicine, University of Florida, Gainesville, FL 32611, USA*
[5] *Department of Materials Science and Engineering, Whiting School of Engineering, Johns Hopkins University, Baltimore, MD 21218, USA*
[6] *Johns Hopkins School of Nursing, Baltimore, MD 21205, USA*
[7] *Department of Molecular and Comparative Pathobiology, Johns Hopkins School of Medicine, Baltimore, MD 21205, USA*
[8] *Department of Biomedical Engineering, Yale University, New Haven, CT 06520, USA*
[9] *Translational Tissue Engineering Center, Johns Hopkins University School of Medicine, Baltimore, MD 21231, USA*

Received: 13 November 2018 / **Revised:** 14 January 2019 / **Accepted:** 15 January 2019

ABSTRACT

Lymph node (LN) targeting through interstitial drainage of nanoparticles (NPs) is an attractive strategy to stimulate a potent immune response, as LNs are the primary site for lymphocyte priming by antigen presenting cells (APCs) and triggering of an adaptive immune response. NP size has been shown to influence the efficiency of LN-targeting and retention after subcutaneous injection. For clinical translation, biodegradable NPs are preferred as carrier for vaccine delivery. However, the selective "size gate" for effective LN-drainage, particularly the kinetics of LN trafficking, is less well defined. This is partly due to the challenge in generating size-controlled NPs from biodegradable polymers in the sub-100-nm range. Here, we report the preparation of three sets of poly(lactic-co-glycolic)-b-poly(ethylene-glycol) (PLGA-b-PEG) NPs with number average diameters of 20-, 40-, and 100-nm and narrow size distributions using flash nanoprecipitation. Using NPs labeled with a near-infrared dye, we showed that 20-nm NPs drain rapidly across proximal and distal LNs following subcutaneous inoculation in mice and are retained in LNs more effectively than NPs with a number average diameter of 40-nm. The drainage of 100-nm NPs was negligible. Furthermore, the 20-nm NPs showed the highest degree of penetration around the paracortex region and had enhanced access to dendritic cells in the LNs. Together, these data confirmed that small, size-controlled PLGA-b-PEG NPs at the lower threshold of about 30-nm are most effective for LN trafficking, retention, and APC uptake after s.c. administration. This report could inform the design of LN-targeted NP carrier for the delivery of therapeutic or prophylactic vaccines.

KEYWORDS

biodegradable nanoparticle, lymph node trafficking, vaccine delivery, nanoparticle size, antigen presenting cells, *in vivo* imaging

1 Introduction

The lymphatic system serves a key role in maintaining fluid balance, and facilitating immune information transfer by localizing and concentrating self or non-self antigens originating from peripheral circulation, and maximizing subsequent processing and presentation of cognate antigens to lymphocytes [1, 2]. The discovery that the majority of antigen presenting cells (APCs) in the draining lymph node (dLN) are immature in nature has shifted the attention of vaccine delivery away from the low density of dendritic cells (DCs) in the periphery to the high density of immature APCs within the dLN [3]. The high density of immature APCs, and naive B-/T-lymphocytes within the dLN makes these secondary lymphatic structures key targets for the delivery of immunomodulatory cues to control or augment systemic immunity [4, 5].

Earlier work using proteins, liposomes, and dendrimers described a size-dependent drainage to the capillaries or lymphatic system after subcutaneous (s.c.) administration [6–8]. These insights were later applied to nanoparticle (NP) delivery of immunomodulatory cargo to lymph nodes as a vaccine delivery platform using both biodegradable and non-degradable polymeric systems, such as poly(propylene-sulfide) [9, 10], and poly(styrene) NPs [11–13], respectively. These studies showed that NP size was a key determinant affecting NP drainage to major dLNs following intradermal (i.d.) or s.c. injection [9, 12, 14]. NPs with an average diameter less than 100-nm can traverse the tissue interstitium by diffusion and convection transport through water-channels in the dense extracellular matrix, past lymphatic endothelium weak cell-cell junctions or a discontinuous basement membrane, and subsequently drain into the LNs where these NPs are taken up preferentially by immature DCs within a few hours to a day [15]. Interstitial inoculation of poly(propylene-sulfide) NPs with an average diameter of 20-nm had greater LN-targeting

Address correspondence to Hai-Quan Mao, hmao@jhu.edu; Rhoel R. Dinglasan, rdinglasan@epi.ufl.edu

ability as well as DC uptake compared to 100-nm NPs [9, 10]. NPs above this threshold are retained at the injection site where peripheral circulating DCs take up the NPs, become activated upon interaction, and drain to the LNs after 48 h [16].

Biodegradable polyesters, e.g., poly(lactic acid) (PLA), poly(glycolic acid) (PGA), poly(ε-caprolactone) (PCL), and their co-polymers, have a long history of clinical use and a good safety track record [17, 18]. Therefore, these materials are preferable choices for making NPs for clinical applications. The use of polyester NPs for LN-targeted delivery of antigens has been limited due to a lack of an effective method that allows for preparation of NPs with a well-controlled size range below 100-nm and a narrow size distribution [17–21]. While NPs smaller than 60-nm are proposed to more efficiently drain to the LNs, it has been difficult to validate this size gating using polyester NPs. Here, we leveraged the advantages of flash nanoprecipitation (FNP) to prepare three batches of small NPs with narrow size distributions (number average sizes: 20-nm, 40-nm, and 100-nm; PDI = 0.12–0.16) using a three-inlet confined impinging jet mixer (CIJM) to mix a solution jet of an amphiphilic diblock polymer (i.e., poly(lactic-co-glycolic acid)-b-poly(ethylene glycol), PLGA-b-PEG) dissolved in a water-miscible organic solvent with water jets under a turbulent mixing condition [22, 23]. We then characterized their size-dependent transport kinetics and retention in different sets of LNs in a mouse model, and evaluated the effect of NP size on their uptake by DCs and macrophages.

2 Experimental section

2.1 Materials

Poly(lactide-co-glycolide)$_{20K}$-b-methoxy poly(ethylene glycol)$_{3K}$ ($PLGA_{20K}$-b-$mPEG_{3K}$) was purchased from PolySciTech®. Cy7.5 carboxylic acid was purchased from Lumiprobe. Alexa488 carboxylic acid, 4',6-diamidino-2-phenylindole (DAPI), and Prolong Diamond Antifade mounting media were purchased from Thermo Fisher Scientific. N,N'-dicyclohexylcarbodiimide (DCC), 4-dimethylaminopyridine (DMAP), acetone, acetonitrile (ACN), methanol, dimethylformamide (DMF), dichloromethane (DCM), tetrahydrofuran (THF), and goat serum were purchased from Sigma-Aldrich. 300 kDa mPEG (modified polyethersulfone) hollow fiber filters were purchased from Spectrum Labs. DC2.4 dendritic cells and all cell media components were purchased from Millipore Sigma (Burlington, MA). Primary and secondary antibodies and related supplies for microscopy were purchased from Fisher Scientific, Biolegend, Thermofisher, Abcam, Biorad Antibodies, and Jackson Immunoresearch as detailed in the methods.

2.2 Mice

SKH1 Elite mice (Charles River) and CD-1 IGS mice (Charles River) at 6–10 weeks old and weighing 20–30 g were used for this study. All studies were done in accordance with protocols approved by the Institutional Animal Care and Use Committee of Johns Hopkins University, an AAALAC-accredited institution.

2.3 Dye labeling of PLGA

Cy7.5 carboxylic acid and Alexa488 carboxylic acid dyes were conjugated with $PLGA_{20K}$-b-$mPEG_{3K}$ by Michael addition. Briefly, the dye in carboxylic acid form (0.4 mg) was dissolved in DMF or DCM at a concentration of 10 mg/mL and 40 μL was added to a 960 μL solution containing 10 mg of $PLGA_{20K}$-b-$mPEG_{3K}$, 0.10 mg of DCC, and 0.53 mg of DMAP. The 1 mL solution was shaken for 18 h in the dark. Post-reaction, the dye labeled $PLGA_{20K}$-b-$mPEG_{3K}$ was dialyzed against 4 L of 50/50 v/v acetone/methanol with changes every 4 h to remove the unreacted dye product. The Cy7.5-$PLGA_{20K}$-b-PEG_{3K} or Alexa488-$PLGA_{20K}$-b-$mPEG_{3K}$ was removed from the dialysis tubing, dried, and reconstituted in THF at 10 mg/mL.

2.4 PLGA-PEG nanoparticle fabrication

Nanoparticles were generated using a three-inlet flash nanoprecipitation device. Two inlet inputs contained only distilled, deionized water (conductivity < 100 μS/cm and TOC < 50 ppb) at pH 7.4 in 20 mL syringes. The third inlet contained 1 mL of 3.184 mg/mL $PLGA_{20K}$-b-$mPEG_{3K}$ containing 54.4 mol% unlabeled $PLGA_{20K}$-b-$mPEG_{3K}$, 14.8 mol% Cy7.5-$PLGA_{20K}$-b-$mPEG_{3K}$, and 30.8 mol% Alexa488-$PLGA_{20K}$-b-$mPEG_{3K}$ dissolved in either ACN (20, 40 nm) or THF (100 nm) in a 5 mL syringe. Nanoparticles of defined size were generated by modulating the organic:water volumetric ratio by changing the relative flow rates of the three input inlets (Table 1) using a NE-4000 Programmable 2 Channel Syringe Pump (SyringePump.com). To remove free polymer and concentrate the nanoparticle samples, nanoparticles were simultaneously concentrated and filtered using a KR2i Tangential Flow Filtration System® (Spectrum Labs) and 300 kDa mPEG hollow fiber filter module unit. To remove any nanoparticles below 100 nm from the 100 nm nanoparticle group, these nanoparticle batches were further separated by size by sucrose gradient (5%, 10%, 15%, and 20% w/v sucrose) and centrifugation (10,000 rpm, 30 min). Nanoparticles in the 20% w/v sucrose cushion were collected, washed with DI water to remove sucrose, and resuspended in 9.5% w/v trehalose prior to *in vitro* and *in vivo* studies.

2.5 Physical characterization

Post-fabrication and concentration, each nanoparticle formulation was diluted to 100 μg/mL NP in 10 mM HEPES buffer (pH 7.2, containing 10 mM NaCl) and its nanoparticle hydrodynamic diameter (number-average) and zeta potential were both measured using a Malvern Zetasizer Nano ZS. The morphology and dry size of each nanoparticle was determined using transmission electron microscopy (TEM) using a Technai FEI-12 TEM electron microscopes. Samples were further diluted and 20 μL aliquots absorbed onto ionized nickel grid covered with carbon films for 30 min at room temperature. The nanoparticle suspension was removed by blotting using Whatman filter paper. The samples were then stained with either 2% w/v uranyl acetate or 1% w/v uranyl formate for 45 s. The grids were blotted to remove excess negative stain and allowed to dry in a chemical hood overnight prior to imaging.

2.6 *In vitro* PLGA-PEG nanoparticle uptake and processing

DC2.4 cells were cultured in RPMI-1640 supplemented with 10% FBS, 1× L-glutamine, 1× non-essential amino acids, 1× HEPES buffer solution, and 0.0054× β-mercaptoethanol as instructed by

Table 1 Fabrication and characterization of each goal $PLGA_{20K}$-b-PEG_{3K} nanoparticle size group

Target size group (nm)	Number average diameter (nm)	Flow rates (Polymer + H_2O + H_2O, mL/min)	Uniformity (PDI)	Zeta potential[a] (mV)
20	17.1 ± 3.1	ACN 5 + 45 + 45	0.12 ± 0.03	−13.1 ± 1.8
40	40.9 ± 1.9	ACN 10 + 5 + 5	0.16 ± 0.02	−10.9 ± 0.7
100	106.9 ± 7.7	THF 2.5 + 1.25 + 1.25	0.13 ± 0.02	−6.8 ± 0.2

[a] Measured in 10 mM HEPES buffer (pH 7.2) with 10 mM NaCl.

the supplier (Millipore-Sigma). For uptake assays, cells were seeded at a density of 50,000 cells/well on poly-l-lysine coated 12 mm #1.5 round cover slips (Electron Microscopy Sciences) in a 24-well tissue culture treated plate. Nanoparticles were diluted to 20 μg/mL in cell medium and 0.5 mL of nanoparticle suspension was provided to cells. At 20 min, 1, 2, and 3 h, cells were washed with 1× PBS to remove free NPs, fixed using 4% paraformaldehyde, washed three times with 1× PBS for 5 min, counterstained using DAPI (1:1,000 in 1× PBS) for 10 min, washed three more times with 1× PBS for 5 min, mounted on microscope slides using ProLong Diamond Antifade mounting media, and allowed to cure in the dark for 24–36 h. Qualitative uptake was determined using a Zeiss LSM 800 confocal microscope. Cells were confirmed to be mycoplasma free before running these assays using a luminescence-based mycoplasma detection assay (Lonza™ MycoAlert™).

2.7 *In vivo* trafficking and retention

Alexa488 and Cy7.5 labeled $PLGA_{20K}$-b-$mPEG_{3K}$ nanoparticles were normalized to 1.5 mg/mL in 9.5% w/v trehalose (Sigma) as measured by a Pearl® Small Animal Imager (Licor). SKH-1 Elite mice (Charles River) were injected with 20 μL of nanoparticle suspension 1 cm below tail-base by subcutaneous injection. Mice were placed inside a Pearl Imager and imaged using the NIR 800 nm channel at 0, 20 min, 1, 2, 3, and 24 h post-injection while briefly under light isoflurane anesthesia. A subset of mice at 3 or 24 h were sacrificed, and lymph nodes and major reticuloendothelial organs were collected and imaged on Parafilm® M film (Fisher Scientific). Post-imaging, lymph nodes were immediately transferred to and immersed in optimal cutting solution (OCT, Fisher Scientific) and snap-frozen in a liquid-nitrogen cooled bath of isopentane (Sigma-Aldrich). Snap-frozen samples were transferred on dry ice to −80 °C storage until later cryosectioning, immunofluorescence staining, and confocal analysis. The Cy7.5-$PLGA_{20K}$-b-$mPEG_{3K}$ signal in each tissue was quantified using Pearl Image Studio Lite Ver 5.2.

2.8 Confocal microscopy

Snap-frozen tissues were sectioned at 6 μm thick sections using a Leica Biosystems cryostat. Samples were fixed with 4% PFA for 15 min and washed with 1× PBS three times for 5 min. Sections were blocked using 5% goat serum in 1× PBS for 1 h. Primary antibody mixture in blocking solution was then incubated with the sample overnight at 4 °C. Primaries include Armenian hamster anti-$CD11c^+$ clone N418 (1:100, Abcam ab33483), rat anti-$CD169^+$ clone MOMA-1 (1:200, Biorad Antibodies MCA947G), Armenian hamster anti-$CD3e^+$ clone 145-2C11 (1:100, Biolegend 100302), and rat anti-$B220^+$ clone RA3-6B2 (1:200, Thermofisher 14-0452-85). The section was washed four times for 5 min with 0.05% Tween-20 1× PBS. Secondary antibodies Cy™3 Affinipure Goat Anti-Armenian Hamster IgG (H+L) (1:100, Jackson Immunoresearch 127-165-160) and Cy™5 Affinipure Goat Anti-Rat IgG (H+L) (1:100, Jackson Immunoresearch 112-165-003) in 5% goat serum in 1× PBS were added for 2 h at room temperature. After four washes with 0.05% Tween-20 1× PBS for 5 min, the sample was stained with DAPI (1:1,000 in 1× PBS) for 10 min and washed four times again with 0.05% Tween-20 1× PBS for 5 min. The slide was dipped in distilled, deionized water to remove residual salts. The sample was mounted using ProLong Diamond Antifade mounting media and a #1.5 coverslip (Fisher Scientific). The sample cured for 24–36 h at room temperature in the dark. Samples were imaged using a Zeiss LSM 800 confocal microscope.

2.9 Structured illumination microscopy

Snap-frozen tissues were sectioned at 6 μm thick sections using a Leica Biosystems cryostat. Tissue sections were fixed with 4% PFA for 15 min and washed with PBS three times for 5 min. Samples were blocked with 1% bovine serum albumin (BSA) in 1× PBS for 30 min, then washed with 1× PBS three times for 5 min. Sections were probed with rabbit anti-AlexaFluor 488 (1:250, ThermoFisher A-11094) and either rat anti-CD86 clone FA-11 (1:250, Biolegend 137001), rat anti-CD169 clone 3D6.112 (1:250, Biolegend 142401), or mouse anti-CD11c clone 3.9 (1:250, Abcam ab11029) in 1× PBS, overnight at 4 °C. Following primary antibody incubation, sections were washed three times with 1× PBS for 5 min, then probed with donkey anti-rabbit Alexa Fluor 488 (1:500, ThermoFisher A-21206), and either goat anti-rat Alexa Fluor 594 (1:500, Abcam ab150160) or goat anti-mouse Alexa Fluor 594 (1:500, ThermoFisher A-11005) in 1× PBS, for 1 h at room temperature. After secondary antibody staining, sections were then washed three times with 1× PBS for 5 min, stained with DAPI (1:1,000 in 1× PBS), for 10 min, washed again with 1× PBS (three times, 5 min each), then mounted using ProLong Diamond Antifade Mountant with DAPI (ThermoFisher P36971) onto 12 mm #1 circle coverslips (Electron Microscopy Sciences 7223101). After 24 h, coverslips were sealed with clear acrylic nail polish, and imaged on a Keyence BZ-X700 All-In-One Inverted Fluorescence Structured Illumination Microscope (Keyence).

2.10 Flow cytometry

DC2.4 cells were seeded at a density of 50,000 cells/well on a 24-well tissue culture treated plate. Nanoparticles were diluted to 20 μg/mL in cell medium and 0.5 mL of nanoparticle suspension was provided to cells. At 20 min, 1, 3, and 24 h, cells were washed with 1× PBS to remove free NPs, harvested using Trypsin-EDTA, washed with ice cold FACS buffer (1× PBS, 10% FBS, 0.1% NaN_3 sodium azide), fixed using 4% paraformaldehyde, and kept at 4 °C until analysis. The nanoparticle signal by a per nanoparticle basis was assessed using a BD FACSCanto.

2.11 Statistical analysis

Data are shown as mean ± standard deviation. Boxplots are plotted showing minimum to maximum data points. All statistical analyses were performed with GraphPad Prism 7.0 software package. Trafficking data was analyzed by non-parametric Kruskal-Wallis test with Dunn's multiple comparison *post-hoc* test to determine differences between groups. The values were considered significantly different at $p < 0.05$. Statistics on graphs were displayed as ns $p > 0.05$, $^*p < 0.05$, $^{**}p < 0.01$, $^{***}p < 0.001$, with $\alpha = 0.05$. All data shown are the result of three or more independently conducted experiments.

3 Results and discussion

Before we assess NP size effect on LN trafficking, DC uptake, processing and presentation of antigen payloads, and immune activation, as well as identify the effective size range for biodegradable $PLGA_{20K}$-b-$mPEG_{3K}$ NPs [24], we first evaluated the effectiveness of the FNP method in preparing size-controlled $PLGA_{20K}$-b-$mPEG_{3K}$ NPs (Fig. 1(a)). By tuning the jet velocity of the three inlet solutions (or water), organic solvent polarity, organic solvent to water ratios, and concentration of the amphiphilic diblock polymer, we obtained conditions that yield polymer solute super-saturation upon rapid and homogenous mixing of water-miscible organic solvent and bulk water, leading to (i) rapid precipitation of the hydrophobic PLGA segment to form polymer nuclei, (ii) relative uniform aggregate growth, and (iii) formation of homogenous NPs [22]. We mapped these experimental parameters and we were able to tune the size and distribution of the NPs (Figs. 1(b) and 1(c)). Three batches of $PLGA_{20K}$-b-PEG_{3K} NPs with number average diameters of 20-, 40-, and 100-nm, respectively, were selected from this NP series (Table 1). After subsequent dialysis, concentration using a tangential flow filtration system, lyophilization in 9.5% w/v trehalose, and reconstitution, these NPs preserve their size and uniformity with negligible batch-to-batch variability and minimum size overlaps among the

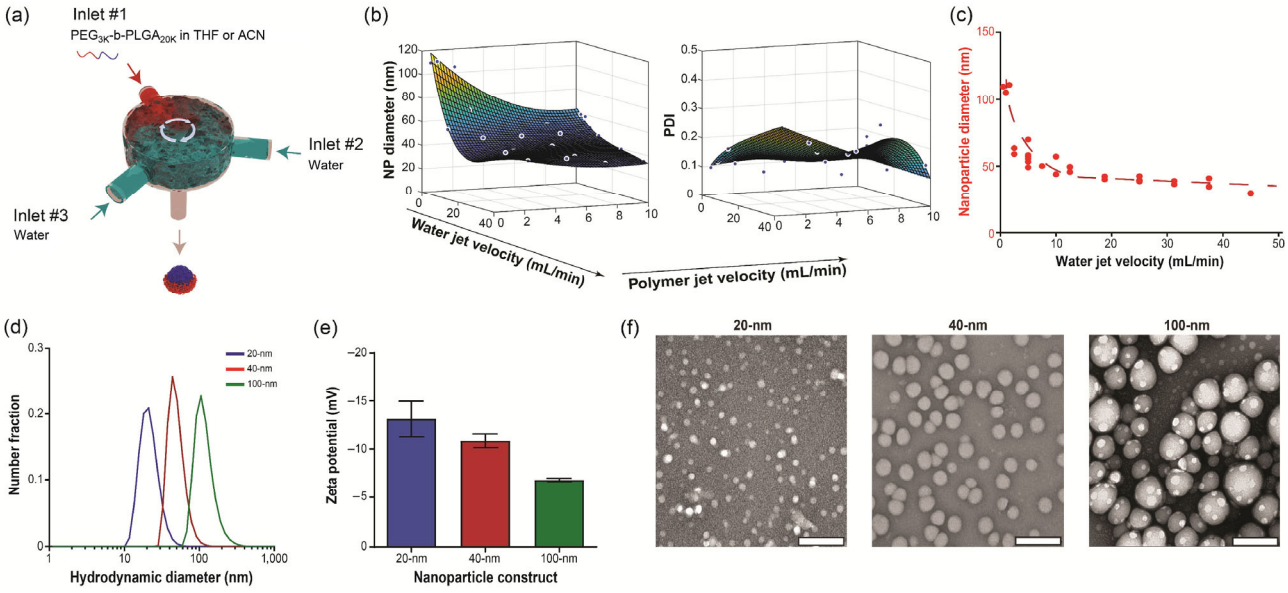

Figure 1 Size-controlled PLGA-b-PEG NPs are prepared by flash nanoprecipitation. (a) CIJM schematic illustrating generation of PLGA-b-PEG NPs by controlled mixing. (b) Control of NP size and PDI by tuning the relative jet velocities of Inlet 1 to Inlets 2 and 3. (c) Orthogonal *x*–*z* projection of (b) demonstrating that NP size was primarily determined by input water jet velocity. (d) Dynamic light scattering (DLS) measurements with number average hydrodynamic diameters. (e) Zeta potential of each NP batch. (f) Transmission electron microscopy confirmed the average hydrodynamic diameters and size distributions for 20, 40, and 100-nm nanoparticles. Scale bar = 200 nm.

three groups (Fig. 1 and Fig. S1 in the Electronic Supplementary Material (ESM)).

The TEM microscopy and dynamic light scattering (Figs. 1(d) and 1(f), and Fig. S1 in the ESM) confirmed the homogeneity of each NP batch and the zeta potential measured in 10 mM HEPES buffer (pH 7.2, with 10 mM NaCl) (Fig. 1(e)) showed that all three sets of NPs carried negative surface charge and became more neutral with increasing size. This trend held when these NPs' zeta potentials were measured in 0.1× PBS and 1× PBS (Figs. S1(b) and S1(c) in the ESM). For imaging purposes, we labeled these NPs with Cy7.5 and Alexa488 conjugated $PLGA_{20K}$-b-$mPEG_{3K}$ at a mol% ratio of 14.8%, 30.8%, and 54.5% unlabeled, respectively, to allow for whole body NP tracking using the Pearl Impulse Imager (LI-COR) and determination of NP distribution within dLNs by fluorescence microscopy.

To better understand the role of size on NP trafficking to the dLNs after s.c. injection, we injected 20-, 40-, or 100-nm NPs (Fig. S2 in the ESM) 1-cm away from the tail base of SKH1 Elite mice, and acquired whole-body NIR images at 20 min, 1, 2, 3, and 24 h post injection. Lymphatic drainage of albumin-hitchhiking dyes (e.g., Evan's Blue) has shown that s.c. injection at the tail-base has a distinct lymphatic drainage path relative to s.c. injection at the footpad [25]. Given that footpad injection introduces greater variability in interstitial pressure and often results in loss of injected sample, we opted to use tail-base administration. For tail-base injections, injected cargoes will go from the injection site either to the iliac LNs or to inguinal LNs, followed by axillary LNs [25]. A similar drainage pattern was seen in our NPs, with a majority of dose going to the inguinal and axillary LNs. (Fig. 2(a)). NP signal was clearly observed in the proximal inguinal dLNs within 20 min post injection for the 20-nm NP group, while the 40-nm NP group had a low level of signal at 3 h post-injection (Fig. 2(a1)). Mice injected with 9.5% w/v trehalose alone served as a vehicle control with no detectable signal (Fig. 2(a2)), validating the specificity of NP signals (Fig. 2(a1)). The 20-nm NP signal was significantly higher than the 40-nm NP signal for all time points tested in all LNs (Fig. 2(b1), and Fig. S3 in the ESM). When NP signal by LN was further delineated, the source of significant difference in NP signal between groups was the proximal inguinal dLNs (Fig. 2(b2)), while statistically insignificant NP signal differences were observed in distal axillary LNs (Fig. 2(b3)). The 100-nm NP group had little drainage from the tail injection site (Fig. 2(a1)), agreeing with previous reports suggesting that 100-nm was the upper size-gate limit for lymphatic drainage due to the effective pore size of interstitium extracellular matrix or size limitations of lymphatic endothelial cells' anchoring filaments upon entering the lymphatic circulation [26]. Despite there being mouse to mouse variation in left/right side lymphatic drainage preference (where the majority of dose would only drain through one side of the lymphatic system for an individual mouse), when all imaged LNs were analyzed in aggregate, there was no significant side bias for tail base s.c. injections for NPs within 20- to 100-nm size range (Fig. 2(b), and Fig. S4 in the ESM).

We noted that the peak 20- and 40-nm NP signals in axillary and inguinal dLNs were observed at 3 h post-injection (Figs. 2(a) and 2(b)). Visualization of iliac drainage of labeled NPs is difficult via ventral *in vivo* whole-body scans but can be re-evaluated following organ harvest. Whole LNs and organs excised and imaged *ex vivo* at 3 and 24 h showed significant differences in signal intensity between each group in the order 20-nm > 40-nm >> 100-nm for both time points (Figs. 3(a) and 3(b)). As noted previously, the majority of bNPs drained to the inguinal and axillary LNs, but a minority also trafficked to iliac LNs. Minimal drainage of 100-nm NPs was noted in this *ex vivo* assay that were otherwise occluded in the whole-body scan (Fig. 3(a)). The total percentage of dosage that drained to the LNs or major reticuloendothelial system (RES) organs vs. those retained at the injection site varied significantly by NP size. An average of 12.4% of injected dose drained to the dLNs for 20-nm NPs compared to 5.1% of 40-nm and 1.0% of 100-nm NP injected dose (Fig. S5 in the ESM). Surprisingly, the percentage of injected dose that drained to the RES organs was not significantly different between 20- and 40-nm size groups (15.4% vs. 15.8%) while 100-nm had less drainage (7.65%) to the RES system due to retention of the majority of the dose at the injection site (Fig. S5 in the ESM). For all groups, the majority of injected dose was retained at the injection site in a size dependent manner, with a greatest proportion of injected dose at injection site for 100-nm NPs, followed by 40-nm and then 20-nm NPs. The same size-dependent manner of passive dLN targeting, RES organ uptake, and retention of injected dose at the injection

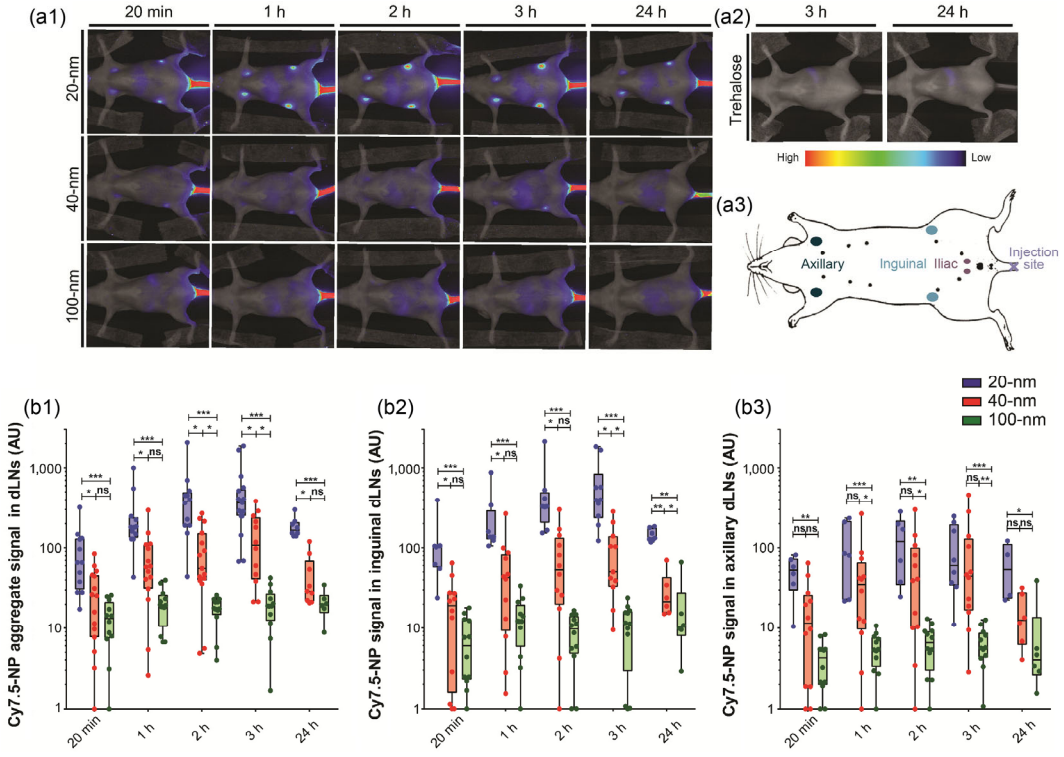

Figure 2 The 20-nm NPs traffic to draining LNs after s.c. tail-base injection. Representative whole-body images (a1) of Cy7.5-labeled NP signal and (a2) 9.5% w/v trehalose vehicle control over a 24 h period. (a3) Mouse schematic detailing major dLNs and injection site location. Quantification of Cy7.5-labeled NP trafficking data over 24 h period in (b1) all visible lymph nodes (inguinal and axillary), (b2) inguinal, and (b3) axillary dLNs alone. SKH1 Elite mice, n = 6–10 for each time point. Data is reflective of at least three independent experiments.

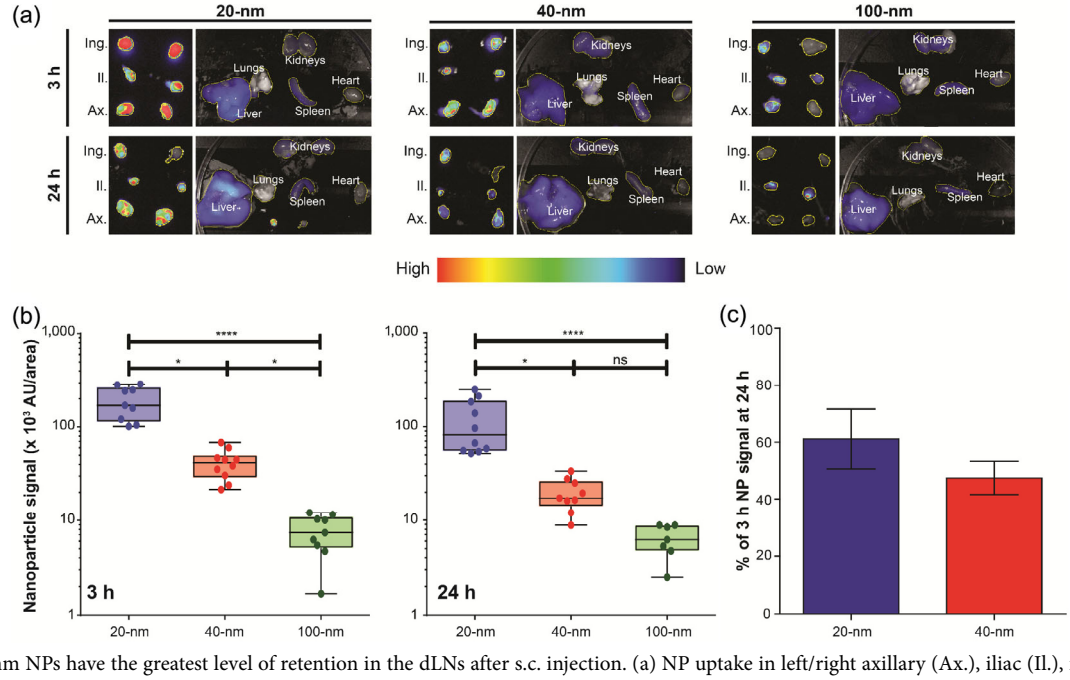

Figure 3 The 20-nm NPs have the greatest level of retention in the dLNs after s.c. injection. (a) NP uptake in left/right axillary (Ax.), iliac (Il.), inguinal (Ing.) dLNs, and mononuclear phagocytic system (lung, liver, spleen, kidneys) after 3 and 24 h post injection. (b) Normalized NP uptake signal in all LNs at 3 and 24 h. SKH1 Elite mice, n = 6–10 for each time point. (c) Retention in dLNs as assessed by the median signal ratio between 3 and 24 h. Data is reflective of at least three independent experiments.

site was observed in an outbred CD-1 IGS mouse model (Fig. S6 in the ESM), suggesting this phenomenon is universal and not mouse model strain dependent.

To further assess NP retention after LN trafficking, we compared the relative signal difference between the maximal NP signal at 3 h to NP signal at 24 h in the dLNs (Fig. 3(c)). A majority (61.1%) of the median signal at 3 h for the 20-nm NP group was retained at the dLNs by 24 h, compared with 47.4% of median signal of the 40-nm NPs at 3 h retained at the dLNs. It is possible that there was a continual drainage of NPs from the injection site between 3 and 24 h, replenishing the NPs that did not retain at the dLNs in a size-dependent manner. Alternatively, there was no further drainage of LNs from the injection site after 3 h due to NP aggregation in the interstitium, and thus further increase in NP signal in the dLN

relied on DC-dependent trafficking. Considering that DC-dependent trafficking is a slow process relative to direct convective transport of NPs [14, 27] and no noticeable change in the signal at the injection site occurred over the 24 h period, this suggests that the 20-nm NPs had better retention in the dLNs over a 24 h period compared to larger NP sizes.

We then examined the effect of NP size on their distribution within the dLNs by confocal microscopy. For the 40- and 100-nm, no significant signal was detected outside of the subcapsular sinus. The 20-nm NPs were likewise mostly relegated to the subcapsular sinus region and were taken up by $CD169^+$ macrophages. However, these 20-nm NPs were able to penetrate into the paracortex region with a majority taken up by DCs as determined by colocalization of Alexa488 signal with $CD11c^+$ DCs (Figs. 4(a) and 4(b)). This enhanced penetration into the paracortex region by 20-nm NPs was interesting given that previous reports suggest that molecules or NPs above 70 kDa or ~ 5-nm are restricted to the periphery of the LNs and can only pass through without interaction with DCs or T-cells in the paracortex region [28]. Molecules smaller than 5-nm can penetrate into the paracortex region as a result of shunting through LN conduits [29, 30]. Molecules or NPs larger than 5-nm can traffic into the paracortex through interaction with subcapsular macrophages if and only if coated with complement. Given that our 20-nm NPs were delivered without antigen cargo or surface nucleophiles for complement activation [31], it is noteworthy that these NPs penetrate deeply into the paracortex region of the dLNs (Fig. 4(a)). According to the DLS size distributions of these 20-nm NPs, 9.2% of the administered NP population was between 6-nm and 10-nm in hydrodynamic diameter, it is likely that the observed penetration was contributed by this fraction of particles through conduit trafficking inside the LNs. Other mechanisms for deeper penetration into the dLN at the size range tested warrants additional investigation within the context of vaccine delivery.

To explore size-dependent uptake of these NPs by antigen presenting cells (APCs), we used confocal microscopy and flow cytometry to assess NP uptake by $CD68^+$ APCs and $CD169^+$ macrophages *in vivo* and DC2.4 DCs *in vitro* over a 3 h time period (Figs. 4(c)–4(e), and Figs. S7 and S8 in the ESM). We observed labeled 20-nm NPs within the cytoplasm of APCs, such as $CD68^+$ DCs/Macrophages (Fig. 4(c)) and dLN-resident $CD169^+$ macrophages (Fig. 4(d)) in the inguinal lymph node at 3 h, suggesting relatively rapid LN penetration and APC uptake of these small, biodegradable NPs as compared to similar sized NPs that have been described previously [9, 10]. In an *in vitro* model we confirmed uptake of NPs by DC2.4 DCs and observed no significant difference between uptake between the 20-, 40-nm groups at all time points, but did observe higher uptake by 100-nm as assessed by confocal microscopy (Fig. 4(e), and Fig. S7 in the ESM) and flow cytometry (Figs. S8 and S9 in the ESM). The 100-nm NP group only had statistically higher uptake than both the 20- and 40-nm groups at 3 h (Fig. S9 in the ESM). For *in vitro* uptake at 3 h, the 100-nm group had 14.8% and 12.7% higher uptake than the 20- and 40-nm groups, respectively, suggesting that in instances were nanoparticle dosing can be guaranteed and is not hindered by drainage kinetics, larger nanoparticles are better for DC uptake. This general trend of increased DC uptake with increased NP size is similar to a recent report using gold NPs [32] and earlier reports using poly(amino acid) NPs [33] and poly(propylene sulfide) (PPS) NPs [34]. Unlike the gold, poly(amino acid), and PPS NP reports, the 20- and 40-nm PLGA-b-PEG NPs had similar uptake rates, suggesting these NPs are being taken up by a similar mechanism. Hirosue, et al. elucidated the uptake mechanism for their PPS NPs (< 100 nm) by incubating these NPs with bone marrow derived dendritic cells in the presence of endocytic and macropinocytic uptake inhibitors. They found that nanoparticles within this size range were taken up primarily by

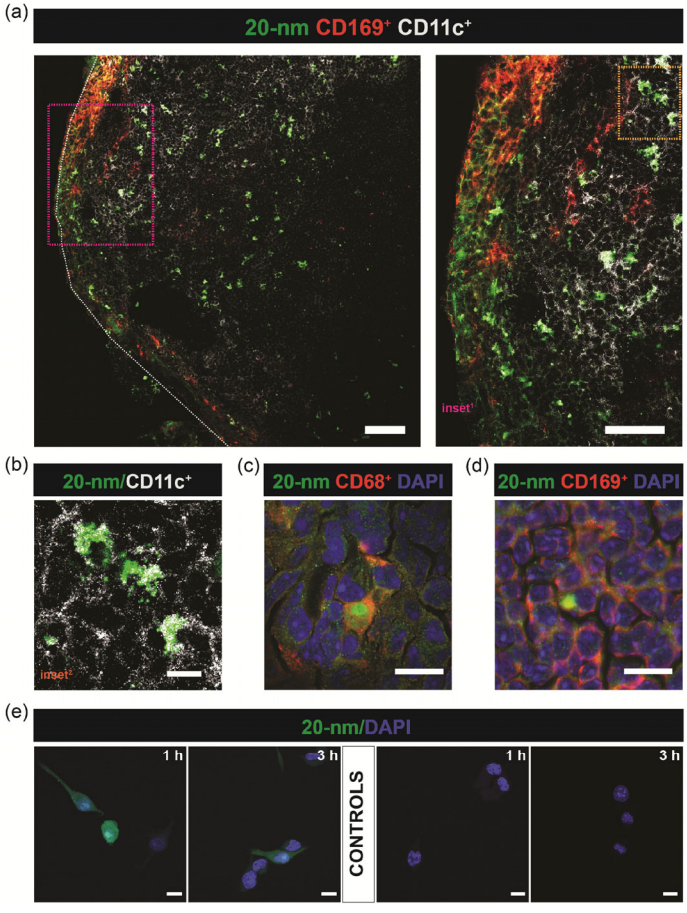

Figure 4 Rapid uptake of 20-nm NPs by antigen presenting cells. (a)–(d) Representative confocal microscopy images of 20-nm NPs in 6-μm inguinal LN sections at peak signal level (3 h after injection). (e) *In vitro* uptake by immortalized DC2.4 mouse dendritic cells was confirmed by confocal microscopy for 20-nm NPs over 3 h. Scale bars: (a) 50 μm, (b)–(e) 10 μm.

endocytosis and less so by macropinocytosis. Kim et al. found that their poly(amino acid) NPs within the 30–100 nm diameter range had similar increasing rates of uptake that correlate with nanoparticle size in bone marrow derived dendritic cells as seen with our nanoparticle system. This report also found that the primary uptake mechanism was endocytosis. Given these results and the fact these nanoparticles have similar size and zeta potential characteristics, we do not anticipate that our PLGA-b-PEG NPs have a different mechanism for uptake. In the PLGA-b-PEG system when tested *in vivo*, the 20- and 40-nm NPs had 12.4- and 5.1-fold higher nanoparticle dose in the draining lymph nodes at 3 h (Fig. S5 in the ESM). The better trafficking of 20- and 40-nm NPs relative to the 100-nm NP group would greatly offset their lower capacity for DC uptake and processing. Meanwhile, the 100-nm NPs will be relegated to the injection site where there is a much lower density of skin-resident DCs, and will likely initiate a less robust immune response within the context of vaccine delivery.

This design dilemma in optimizing NP size to increase drainage kinetics while also enhancing DC uptake has been reviewed extensively in the literature [35]. As discussed by Jiang et al., NP size, surface charge, and PEGylation are vehicle characteristics that can be tuned to optimize lymph node delivery. This report presenting the PLGA-b-PEG system likewise optimizes size (20-nm), surface charge (20-nm is most negative, and this confers an advantage in drainage kinetics), and PEGylation (100% of nanoparticle surface). Unlike other delivery systems previously reported, the PLGA-b-PEG system has little difference in DC uptake between NPs of large (100-nm) and small (20-nm) size. With this data in mind, this system may have an advantage over other systems reported in the literature by

having small, negatively charged, PEGylated NPs that have enhanced lymph node targeting and similar dendritic cell uptake relative to larger NP sizes. Further work is required to detail the immune response elicited by antigen loaded or surface conjugated NPs of various sizes generated by this platform to determine if this advantage translates into a more robust immune response.

Since the hydrodynamic diameter appears to be the major determinant for LN drainage as previously reported and further supported by this study, we aimed to further define the size gating for lymphatic drainage. We performed an analysis of the whole body and *ex vivo* assessments of NP drainage and retention, by correlating the differences in NP signal to proportions of each NP population in specific, pre-defined size gates as determined by DLS distribution. This method of analysis assumes that only a fraction of the NP population below a specific size limit is capable of draining to the dLNs and contributes to the NP signal in each set of dLNs. We normalized the NP mean signal for each group to the mean signal of the 20-nm NPs for each corresponding time point up to 3 h and excluded the 24 h time point to remove signal attributed to DC-mediated NP trafficking. In addition, we generated another nanoparticle group with a number average of 30-nm to serve as an intermediate size between the 20- and 40-nm groups. We then compared these signal ratios to the fractions of NPs within a specific size gate (Fig. S10 in the ESM), and revealed that the mean signal ratios for NPs between 20- and 40-nm, and between 20- and 30-nm, at 20 min, 1, 2, and 3 h matched well with the NP fractions of size smaller than 33-nm between 20- and 40-nm NP groups and 20- and 30-nm groups, respectively. This finding assumes that only NPs with size below 33-nm in each NP group (20-, 40-, 100-nm) can drain by convective transport to the dLNs after s.c. injection. Since the 40-nm group has a smaller proportion of its population below this upper size gate, and 100-nm has none in this range, compared to the 20-nm group, this would explain the relative differences in drainage, retention, and NP distribution of each size-controlled NP group.

4 Conclusion

In summary, we screen-tested a range of experimental parameters and demonstrated that biodegradable PLGA-b-PEG NPs could be produced with well-controlled size and narrow size distribution using the FNP method. This process is amenable to large-scale production with minimal batch-to-batch variability and high translation potential for therapeutic or prophylactic vaccine delivery. Using three lyophilized NP preparations with number average diameters of 20- , 40-, and 100-nm prepared with this method, we examined the trafficking kinetics and retention to the dLNs after s.c. injection, and found that 20-nm NPs were optimal for its quick drainage kinetics, superior retention, and enhanced penetration into the dLNs in comparison with 40- and 100-nm NPs. In an *in vitro* uptake setting where nanoparticle uptake is decoupled from *in vivo* trafficking kinetics and distribution within the lymph node, no significant difference was observed between the 20- and 40-nm NPs, while 100-nm NPs had slightly enhanced uptake (14.8% and 12.7% increase in uptake, respectively) after 3-h as assessed by confocal microscopy and flow cytometry. Meanwhile *in vivo*, the 20- and 40-nm NPs had 12.4- and 5.1-fold higher NP dose in the draining lymph nodes relative to the 100-nm NP at 3-h post-s.c. administration. This insight highlights that the limiting factor for successful delivery of nanoparticle therapeutics of this size range (< 100 nm) is the drainage kinetics, lymph node penetration and distribution, and retention over time. A simple proportional analysis of the relative NP signal in the dLNs and NP size distribution revealed a narrower NP size gate of 33-nm within a NP population responsible for the relative amount of NP signal detected in dLNs. This finding would need to be replicated in other nanoparticle systems to determine if this upper size gate is generalizable to all platforms regardless of material composition. This work provides further insights into the size limit of NPs for LN-targeted vaccine delivery, suggesting that NPs smaller than 30 nm in diameter exhibit optimal drainage kinetics and retention.

Acknowledgements

This work was funded by support from the National Institutes of Health (Nos. R01-AI114609 and T32-OD11089) and NSF GRFP (No. DGE1746891). Partial support was received from the University of Florida Emerging Pathogens Institute.

Electronic Supplementary Material: Supplementary material (additional details of nanoparticle fabrication and physical characterization, nanoparticle drainage kinetics and biodistribution, and *in vitro* nanoparticle uptake assays) is available in the online version of this article at https://doi.org/10.1007/s12274-019-2301-3.

References

[1] Trevaskis, N. L.; Kaminskas, L. M.; Porter, C. J. H. From sewer to saviour-targeting the lymphatic system to promote drug exposure and activity. *Nat. Rev. Drug Discov.* **2015**, *14*, 781–803.

[2] Willard-Mack, C. L. Normal structure, function, and histology of lymph nodes. *Toxicol. Pathol.* **2006**, *34*, 409–424.

[3] Wilson, N. S.; El-Sukkari, D.; Belz, G. T.; Smith, C. M.; Steptoe, R. J.; Heath, W. R.; Shortman, K.; Villadangos, J. A. Most lymphoid organ dendritic cell types are phenotypically and functionally immature. *Blood* **2003**, *102*, 2187–2194.

[4] Swartz, M. A.; Hubbell, J. A.; Reddy, S. T. Lymphatic drainage function and its immunological implications: From dendritic cell homing to vaccine design. *Semin. Immunol.* **2008**, *20*, 147–156.

[5] Tostanoski, L. H.; Chiu, Y.-C.; Gammon, J. M.; Simon, T.; Andorko, J. I.; Bromberg, J. S.; Jewell, C. M. Reprogramming the local lymph node microenvironment promotes tolerance that is systemic and antigen specific. *Cell Rep.* **2016**, *16*, 2940–2952.

[6] Supsersaxo, A.; Hein, W. R.; Steffen, H. Effect of molecular weight on the lymphatic absorption of water-soluble compounds following subcutaneous administration. *Pharm. Res.* **1990**, *7*, 167–169.

[7] Oussoren, C.; Storm, G. Liposomes to target the lymphatics by subcutaneous administration. *Adv. Drug Deliv. Rev.* **2001**, *50*, 143–156.

[8] Kaminskas, L. M.; Porter, C. J. H. Targeting the lymphatics using dendritic polymers (dendrimers). *Adv. Drug Deliv. Rev.* **2011**, *63*, 890–900.

[9] Reddy, S. T.; Rehor, A.; Schmoekel, H. G.; Hubbell, J. A.; Swartz, M. A. *In vivo* targeting of dendritic cells in lymph nodes with poly(propylene sulfide) nanoparticles. *J. Control. Release* **2006**, *112*, 26–34.

[10] Reddy, S. T.; van der Vlies, A. J.; Simeoni, E.; Angeli, V.; Randolph, G. J.; O'Neil, C. P.; Lee, L. K.; Swartz, M. A.; Hubbell, J. A. Exploiting lymphatic transport and complement activation in nanoparticle vaccines. *Nat. Biotechnol.* **2007**, *25*, 1159–1164.

[11] Mottram, P. L.; Leong, D.; Crimeen-Irwin, B.; Gloster, S.; Xiang, S. D.; Meanger, J.; Ghildyal, R.; Vardaxis, N.; Plebanski, M. Type 1 and 2 immunity following vaccination is influenced by nanoparticle size: Formulation of a model vaccine for respiratory syncytial virus. *Mol. Pharm.* **2007**, *4*, 73–84.

[12] Fifis, T.; Gamvrellis, A.; Crimeen-Irwin, B.; Pietersz, G. A.; Li, J.; Mottram, P. L.; McKenzie, I. F.; Plebanski, M. Size-dependent immunogenicity: Therapeutic and protective properties of nano-vaccines against tumors. *J. Immunol.* **2004**, *173*, 3148–3154.

[13] Kumar, S.; Anselmo, A. C.; Banerjee, A.; Zakrewsky, M.; Mitragotri, S. Shape and size-dependent immune response to antigen-carrying nanoparticles. *J. Control. Release* **2015**, *220*, 141–148.

[14] Manolova, V.; Flace, A.; Bauer, M.; Schwarz, K.; Saudan, P.; Bachmann, M. F. Nanoparticles target distinct dendritic cell populations according to their size. *Eur. J. Immunol.* **2008**, *38*, 1404–1413.

[15] Randolph, G. J.; Angeli, V.; Swartz, M. A. Dendritic-cell trafficking to lymph nodes through lymphatic vessels. *Nat. Rev. Immunol.* **2005**, *5*, 617–628.

[16] Li, X. R.; Sloat, B. R.; Yanasarn, N.; Cui, Z. R. Relationship between the size of nanoparticles and their adjuvant activity: Data from a study with an improved experimental design. *Eur. J. Pharm. Biopharm.* **2011**, *78*, 107–116.
[17] Chaney, E. J.; Tang, L.; Tong, R.; Cheng, J. J.; Boppart, S. A. Lymphatic biodistribution of polylactide nanoparticles. *Mol. Imaging* **2010**, *9*, 153–162.
[18] Rao, D. A.; Forrest, M. L.; Alani, A. W. G.; Kwon, G. S.; Robinson, J. R. Biodegradable PLGA based nanoparticles for sustained regional lymphatic drug delivery. *J. Pharm. Sci.* **2010**, *99*, 2018–2031.
[19] Zheng, S. S.; Qin, T.; Lu, Y.; Huang, Y. F.; Luo, L.; Liu, Z. G.; Bo, R. N.; Hu, Y. L.; Liu, J. G.; Wang, D. Y. Maturation of dendritic cells *in vitro* and immunological enhancement of mice *in vivo* by pachyman-and/or OVA-encapsulated poly(D, L-lactic acid) nanospheres. *Int. J. Nanomedicine* **2018**, *13*, 569–583.
[20] Zhang, W. F.; Wang, L. Y.; Liu, Y.; Chen, X. M.; Liu, Q.; Jia, J. L.; Yang, T. Y.; Qiu, S. H.; Ma, G. H. Immune responses to vaccines involving a combined antigen-nanoparticle mixture and nanoparticle-encapsulated antigen formulation. *Biomaterials* **2014**, *35*, 6086–6097.
[21] Maldonado, R. A.; LaMothe, R. A.; Ferrari, J. D.; Zhang, A. H.; Rossi, R. J.; Kolte, P. N.; Griset, A. P.; O'Neil, C.; Altreuter, D. H.; Browning, E. et al. Polymeric synthetic nanoparticles for the induction of antigen-specific immunological tolerance. *Proc. Natl. Acad. Sci. USA* **2015**, *112*, E156–E165.
[22] Johnson, B. K.; Prud'homme, R. K. Mechanism for rapid self-assembly of block copolymer nanoparticles. *Phys. Rev. Lett.* **2003**, *91*, 118302.
[23] Saad, W. S.; Prud'homme, R. K. Principles of nanoparticle formation by flash nanoprecipitation. *Nano Today* **2016**, *11*, 212–227.
[24] Xiang, S. D.; Scholzen, A.; Minigo, G.; David, C.; Apostolopoulos, V.; Mottram, P. L.; Plebanski, M. Pathogen recognition and development of particulate vaccines: Does size matter?. *Methods* **2006**, *40*, 1–9.
[25] Harrell, M. I.; Iritani, B. M.; Ruddell, A. Lymph node mapping in the mouse. *J. Immunol. Methods* **2008**, *332*, 170–174.
[26] Reddy, S. T.; Berk, D. A.; Jain, R. K.; Swartz, M. A. A sensitive *in vivo* model for quantifying interstitial convective transport of injected macromolecules and nanoparticles. *J. Appl. Physiol.* **2006**, *101*, 1162–1169.
[27] Tomura, M.; Hata, A.; Matsuoka, S.; Shand, F. H. W.; Nakanishi, Y.; Ikebuchi, R.; Ueha, S.; Tsutsui, H.; Inaba, K.; Matsushima, K. et al. Tracking and quantification of dendritic cell migration and antigen trafficking between the skin and lymph nodes. *Sci. Rep.* **2014**, *4*, 6030.
[28] Thomas, S. N.; Schudel, A. Overcoming transport barriers for interstitial-, lymphatic-, and lymph node-targeted drug delivery. *Curr. Opin. Chem. Eng.* **2015**, *7*, 65–74.
[29] Sixt, M.; Kanazawa, N.; Selg, M.; Samson, T.; Roos, G.; Reinhardt, D. P.; Pabst, R.; Lutz, M. B.; Sorokin, L. The conduit system transports soluble antigens from the afferent lymph to resident dendritic cells in the T cell area of the lymph node. *Immunity* **2005**, *22*, 19–29.
[30] Roozendaal, R.; Mempel, T. R.; Pitcher, L. A.; Gonzalez, S. F.; Verschoor, A.; Mebius, R. E.; von Andrian, U. H.; Carroll, M. C. Conduits mediate transport of low-molecular-weight antigen to lymph node follicles. *Immunity* **2009**, *30*, 264–276.
[31] Phan, T. G.; Grigorova, I.; Okada, T.; Cyster, J. G. Subcapsular encounter and complement-dependent transport of immune complexes by lymph node B cells. *Nat. Immunol.* **2007**, *8*, 992–1000.
[32] Kang, S.; Ahn, S.; Lee, J.; Kim, J. Y.; Choi, M.; Gujrati, V.; Kim, H.; Kim, J.; Shin, E. C.; Jon, S. Effects of gold nanoparticle-based vaccine size on lymph node delivery and cytotoxic T-lymphocyte responses. *J. Control. Release* **2017**, *256*, 56–67.
[33] Kim, H.; Uto, T.; Akagi, T.; Baba, M.; Akashi, M. Amphiphilic poly(amino acid) nanoparticles induce size-dependent dendritic cell maturation. *Adv. Funct. Mater.* **2010**, *20*, 3925–3931.
[34] Hirosue, S.; Kourtis, I. C.; van der Vlies, A. J.; Hubbell, J. A.; Swartz, M. A. Antigen delivery to dendritic cells by poly(propylene sulfide) nanoparticles with disulfide conjugated peptides: Cross-presentation and T cell activation. *Vaccine* **2010**, *28*, 7897–7906.
[35] Jiang, H.; Wang, Q.; Sun, X. Lymph node targeting strategies to improve vaccination efficacy. *J. Control. Release* **2017**, *267*, 47–56.